SSNMR confirms silicate ion substitution in the apatitic structure of 0.8wt% Si hydroxyapatite

Marc-Krystelle Mafina[1,2,*], Rory M. Wilson[3], Gregory J. Rees[4], Peter Gierth[5], Alice C. Sullivan[6], Karin A. Hing[2]

Academic Editor(s): Evgeni B. Starikov, Raul. D. S. G. Campilho

Abstract

This study investigates the structural location of silicon present in 'silicate-substituted' apatite. It has been hypothesized that silicon is present in the form of silicate groups site-specifically substituted in the hydroxyapatite lattice for phosphate groups, or that there may be an amorphous silicon-rich phase in the vicinity of the grain boundaries. Solid-state nuclear magnetic resonance (SSNMR) spectroscopy was carried out to view the elemental interactions using phosphorus (^{31}P) and silicon (^{29}Si) probes to confirm or refute the presence of silicate groups in relation to phosphate groups in the bulk material structure. The analysis was performed on stoichiometric hydroxyapatite (HA) and silicate-substituted hydroxyapatite (SA) with a nominal silicon content of 0.8wt%, in as-precipitated, calcined (700°C), and sintered (1,250 and 1,300°C, respectively) powder forms. XRD confirmed all forms of powder were phase pure. FTIR confirmed both hydroxyl and phosphate group functionalities in all forms of HA and SA, while silicate group functionality was only observed in all forms of SA. SSNMR using ^{31}P- and ^{29}Si-coupled probes demonstrated that as the crystallinity of the powders increased from the precipitate to the sintered form, the signal associated with the presence of a silicate group in the phosphate environment developed as the crystal structure became more ordered. These results support the hypothesis that in SA containing 0.8wt% silicon, silicate groups are site-specifically substituted in the hydroxyapatite lattice for phosphate groups. This observation may be key to understanding the mechanisms by which the introduction of 0.8wt% silicon enhances bone regeneration in apatitic bone graft substitute materials.

Citation: Mafina M-K, Wilson RM, Rees GJ, Gierth P, Sullivan AC, Hing KA. SSNMR confirms silicate ion substitution in the apatitic structure of 0.8wt% Si hydroxyapatite. *Academia Materials Science* 2023;1. https://doi.org/10.20935/AcadMatSci6121

1. Introduction

Phase-pure silicate-substituted hydroxyapatite (SA), containing 0.8wt% silicon, has been shown to be highly efficacious as a biomaterial for synthetic bone graft substitutes (SBGs) in both pre-clinical and clinical settings [1–4].

It has been proposed that, as compared to phase-pure stoichiometric hydroxyapatite (HA), which is silicon-free ($Ca_{10}(PO_4)_6(OH)_2$), the enhanced bioactivity of SA may be linked to the introduction of silicon as either a direct or an indirect consequence of the change in chemistry. Building on the work of Carlisle [5, 6] and Schwarz [7, 8], who identified silicon to be an essential element for bone and connective tissue development and health, combined with the development of Bioglass™ by Hench [9] and subsequent studies that appeared to link enhanced bioactivity directly to the release of bioavailable silicon

and its action on the metabolism and development of bone forming cells [10], silicon-substituted apatites were developed with the anticipation that incorporation of silicon would enhance the bioactivity of stoichiometric hydroxyapatite [11]. A number of *in vitro* and *in vivo* studies not only confirmed this hypothesis [12–15], but also identified a dose-dependent effect of silicon incorporation with an optimum performance observed for SA containing 0.8wt% silicon [1, 16–18]. Various hypotheses were developed to explain this behavior, including that enhanced bioactivity was linked to the direct action of bioavailable silicon ions on bone [cell] metabolism [12, 16], and/or the effect of silicon incorporation on dissolution and surface reactivity [12], and/or the influence of silicon incorporation into the apatite lattice as silicate groups substituted for phosphate groups on SA physiochemistry and subsequent interaction with biological molecules [19–23].

[1]PerkinElmer AES (UK) Ltd, Buckinghamshire HP9 2FX, United Kingdom.
[2]School of Engineering and Materials Science, Queen Mary University of London, London E1 4NS, United Kingdom.
[3]X-ray Diffraction Facility, Centre for Materials Research, Queen Mary University of London, London E1 4NS, United Kingdom.
[4]Materials NMR/MRI, University of Oxford, Oxfordshire OX1 2JD, United Kingdom.
[5]Bruker Biospin, NMR Centre, Coventry CV4 9GH, United Kingdom.
[6]School of Biological and Chemical Science, Queen Mary University of London, London E1 4NS, United Kingdom.
*email: marc-krystelle.mafina@perkinelmer.com

While various studies have performed basic chemical characterization to confirm phase purity, elemental composition and the impact of silicon incorporation on various parameters of dissolution, surface reactivity, and physiochemistry [1, 11, 12, 16–18, 24–26], no study has directly confirmed whether the silicon is incorporated in the apatite lattice via site-specific substitution of silicate ions for phosphate ions, thus providing a mechanism for control of surface physiochemistry, solubility, and reactivity, or as an amorphous silicon-rich phase at the grain boundaries providing a source of bioavailable silicon, potentially increasing dissolution and surface reactivity. Positive identification of site-specific substitution of silicate for phosphate would help clarify that the enhanced bioactivity could be attributed directly to changes in hydroxyapatite physiochemistry rather than the presence of bioavailable amorphous silicon.

In previous studies, conventional methods of polycrystalline ceramic characterization such as powder X-ray diffraction (XRD), Fourier transform infrared-photoacoustic spectroscopy (FTIR-PAS), and X-ray fluorescence (XRF) were employed to confirm phase purity, ionic group functionality, and elemental composition. XRD is the principle technique used to assess phase purity, acknowledged to be able to resolve the presence of crystalline second phases down to levels of 1wt%, and aside from the fact that XRD is, by its nature, a technique suited to the analysis of materials with a certain degree of crystalline order, it is accepted that powder XRD sensitivity can be limited when determining the presence of 'impurity' ions in apatites at low percentages compared to single crystal XRD [27, 28]. In the case of silicate-substituted apatites, the use of XRD data to assess changes in the lattice and parameters may not be conclusive because of the proximity of silicon (Si) to phosphorus (P) in the periodic table. Moreover, any bulk analysis of the sample by XRD is limited by the electron beam penetration depth and the incident beam voltages used during the analysis, and thus XRD is often associated with surface-only (up to ~1.7 μm) determination [29].

Solid-state nuclear magnetic resonance (SSNMR) is an efficient probing technique of local structures in both highly disordered and crystalline materials. The disorder and chemical ambiguity of substituted apatites make SSNMR a particularly attractive analysis technique for solving the chemical environments in these materials. This is related to the fact that SSNMR probes local structure and long-range order is not required, which is particularly advantageous when studying apatites with low-level substitutions, likely to give only local atomic site distributions in relation to the presence of any substituting ions. For example, a study completed by Isobe et al. [30] demonstrated that multiple phosphorus sites were present in hydroxyapatite due to structural disorder caused by defects and ionic substitutions [30], while Laurencin and co-workers [31, 32] used SSNMR to confirm the existence of two calcium sites in the structure which have been determined to be a nine co-ordinate site Ca(I) and seven co-ordinate site Ca(II). Furthermore, the study of Gasqueres et al. [33], exploring the use of $^1H/^{29}Si$ cross-polarization magic angle spinning (CPMAS) SSNMR to investigate the location of silicon species in silicate-substituted multi-phase apatite-based calcium-phosphates doped with 4.6wt% silicon, demonstrated the technique's ability to confirm whether the substituted silicate species present were taken up inside or outside the apatite structure [33]. Additionally, Andreev et al. used a combination of SSNMR techniques to gain insight into both the crystal structure and phase composition of silicocarnotite ($Ca_5(PO_4)_2SiO_4$)–based bioceramics, including the nature of the silicon environment [34].

Here we utilize silicon-29 (^{29}Si) and phosphorus-31 (^{31}P) CPMAS SSNMR to corroborate the location of the silicon environments in silicate-substituted apatite containing 0.8wt% silicon as compared to stoichiometric apatite.

2. Materials and methods

2.1. Phase-pure stoichiometric hydroxyapatite (HA) and silicate-substituted hydroxyapatite (SA) synthesis

Stoichiometric hydroxyapatite (HA) and silicate-substituted hydroxyapatite (SA) with a silicon content of 0.8wt% Si were synthesized using the aqueous precipitation route described by Gibson et al. [11], based on the method for HA synthesis as described by Akao et al. [35] where parity was maintained between the number of moles of orthophosphoric acid (H_3PO_4) required for the synthesis of stoichiometric hydroxyapatite (HA) and the number of moles of [H_3PO_4 + silicon acetate (Si(CH_3COO)$_4$)] in the SA precipitation while keeping the number of moles of calcium hydroxide Ca(OH)$_2$ constant, thereby maintaining the Ca/(Si+P) ratio as 1.67 (**Figure 1**).
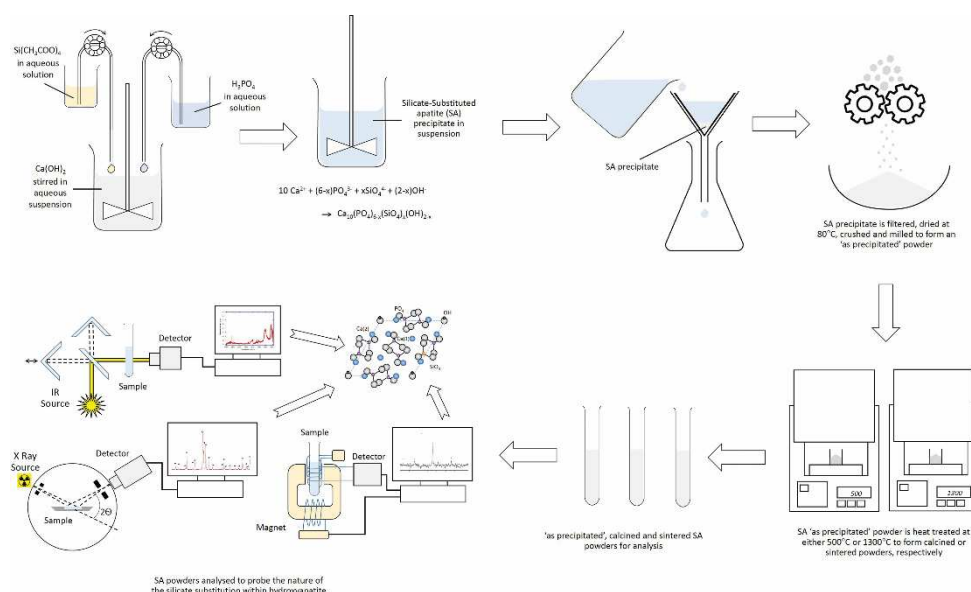

Figure 1 • Schematic of HA & SA powder production for chemical structural analysis.

2.2. Filtering, drying, calcining, and sintering powder

The precipitate was filtered using a horizontal filter press at a pressure of 600 MPa (PALL, Portsmouth, UK, 600 mm horizontal press). The filter cake was dried at 80°C and disk milled to a nominal particle size of 300 μm (Retsch, Haan, Germany, DM150) to produce as-precipitated HA and SA powders. Samples of the as-precipitated powders were then further heat treated either at 700°C in a dry air atmosphere for four hours to produce calcined HA and SA powder samples, or at 1,250°C in a dry air atmosphere for two hours to produce sintered HA powder samples, or at 1,300°C in a dry air atmosphere for two hours to produce sintered SA powder samples, all in a Carbolite Muffle RHF1600 furnace (Carbolite, Hope Valley, UK) (**Figure 1**).

2.3. X-ray fluorescence (XRF) spectroscopy

XRF analysis was performed at Lucideon (Stoke-on-Trent, UK) using a Panalytical XRF spectrometer (Malvern Panalytical, Malvern, UK).

2.4. X-ray diffraction (XRD)

XRD patterns were obtained using X'Pert Pro PW3064/60 (Panalytical, Almelo, Netherlands) with CuK$_{\alpha 1}$ (λ = 1.5406 nm) and CuK$_{\alpha 2}$ (λ = 1.5444 nm) radiation operating at 45 kV and 40 mA. Data were collected by using an X'Celerator RTMS detector continuously over a 2θ range of 5° to 120°, with a step size of 0.0334° and a dwell time of 200 s. Crystallographic parameters were obtained using the XRD diffractograms in conjunction with the following three programs. (1) Xpert HighScore Plus software v2.0 2008 along with the ICDD database was used to establish a reference of the unit cell volume, and the values for the a, b, and c axes using the peak list with the Miller indices of known stoichiometric HA. (2) Pickpx2 software (developed in-house, UK) enabled $xrdml$ and uxd files of the XRD data to be converted into corresponding 2θ values and their d-spacing along with peak intensities. (3) The UnitCellWin software 1997 (developed by Holland and Redfern [36], UK) evaluated all information (Miller indices and 2θ data) and calculated the unit cell parameters ($a = b \neq c$ and cell volume).

2.5. Fourier transform infrared-photoacoustic spectroscopy (FTIR-PAS)

FTIR-photoacoustic spectroscopy (PAS) spectra were obtained using a Thermo Nicolet 8700 spectrometer (Thermo Scientific, Horsham, UK) in conjunction with a PA Cell-MTEC Model 200 with a KRS-5 sample chamber window (MTEC, Ames, US). Spectra were obtained at a resolution of 4 cm^{-1}, averaging 128 scans, operating from 4,000 to 400 cm^{-1}. The sample chamber of the PAS cell was purged with helium gas prior to and during the analysis.

2.6. Solid-state nuclear magnetic resonance (SSNMR)

All SSNMR experiments were performed on a Bruker Avance III HD (Bruker, Coventry, UK) console with a magnet field of, B$_0$, 11.7 T (corresponding to a ^{1}H frequency of 500.13 MHz) standard bore Ascend magnet. The obtained data were processed using the Topspin 3.2 software package. A 4 mm double air bearing standard bore magic angle spinning probe was used giving a maximum spinning frequency of 15 kHz. ^{31}P MAS spectra were achieved at a spinning frequency of 10 kHz at a Larmor frequency of 202.56 MHz. All results were referenced to the secondary standard of ammonium dihydrogen phosphate (δ_{iso} ADP, s = 0.9 ppm with respect to δ_{iso} H$_3$PO$_4$, aq = 0 ppm). A relaxation time of 30 seconds was found to be sufficient, and a 4 μs pulse width was determined. Both CPMAS with proton decoupling (^{1}H decoupling at 100 kHz) and proton-decoupled one-pulse (HPDEC) experiments were performed to give information on the proximity of the phosphorus sites to the neighboring nuclei. ^{29}Si CPMAS (4 kHz) NMR data were obtained at a Larmor frequency of 99.99 MHz. All spectra were referenced to the mineral Kaolinite (δ_{iso} = −93 ppm with respect to δ_{iso} TMS, l = 0 ppm). A 4 ms 50% ramped pulse was used during the contact time, and a 10-second recycle delay was deduced to be sufficient for proton relaxation.

3. Results

3.1. X-ray fluorescence (XRF) spectroscopy

The results of the XRF analysis of sintered HA and SA powders are shown in **Table 1**.

For the stoichiometric HA, the design Ca/P and Ca/(P + Si) molar ratios were identical (1.67), as would be expected for silicon-free samples and showed good agreement with the values measured by XRF (1.68).

For the SA, the design Ca/P molar ratio of (1.76) was higher than the design value for stoichiometric HA reflecting a decrease in the phosphorus content to compensate for the addition of silicon, such that the design Ca/(P + Si) molar ratio in the SA retained parity with the Ca/P molar ratio of stoichiometric HA powders (1.67). There was a good agreement between the design and XRF-measured Ca/(P + Si) molar ratios of SA, and between the design and XRF-measured Ca/P molar ratios. XRF analysis of the levels of silicon in the samples also demonstrated only trace levels of silicon to be found in the stoichiometric HA and a good agreement between the design and measured values of silicon in the SA.

Table 1 • Design and measured (by XRF) molar ratios and wt% silicon and silicate levels for HA and SA powders

	Ca/P molar ratio		Ca/(P+Si) molar ratio		wt% Si		wt% SiO$_4$$^{4-}$	
	Design	Measured	Design	Measured	Design	Measured	Design	Measured
HA	1.67	1.68	1.67	1.68	0	<0.01	0	<0.01
SA	1.76	1.76	1.67	1.68	0.80	0.81	2.62	2.64

3.2. X-ray diffraction (XRD)

XRD confirmed the phase purity of both the HA and SA powder samples (**Figure 2a**, **b**), with all peaks corresponding to those of the ICDD pattern for stoichiometric hydroxyapatite, and no additional peaks were observed to indicate the presence of second phases such as β-TCP or CaO [37, 38]. As expected, the patterns obtained for the precipitate and calcined powders showed broad peaks with relatively low intensity, suggesting that these powders possessed a small crystallite size or reduced stoichiometry resulting in a relatively low level of crystallinity,

whereas the patterns obtained for the sintered powders were significantly sharper, indicating a greater degree of crystallinity or order that may accompany crystallite growth and/or ripening in response to the heat treatment.
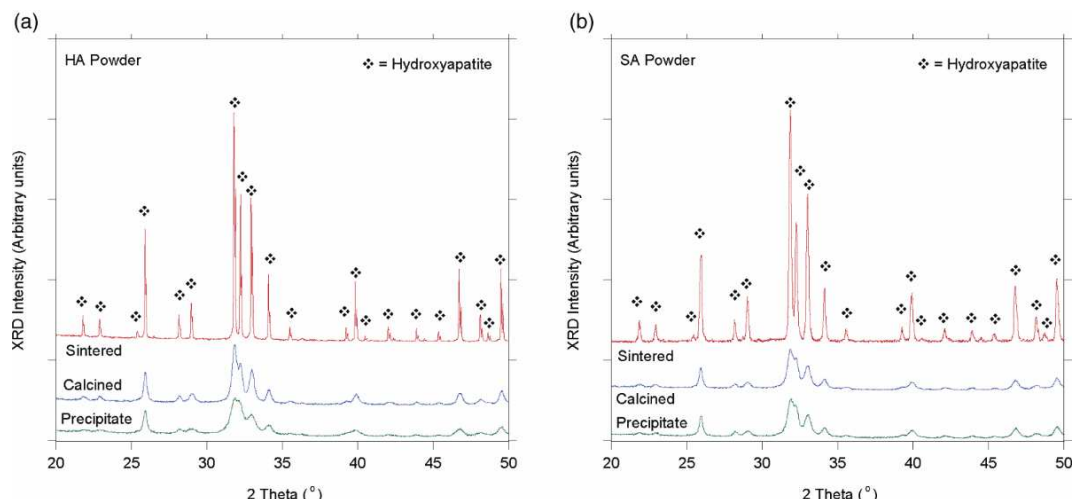

Figure 2 • XRD patterns of (a) HA and (b) SA powder samples.

The effect of the silicon substitution on the crystallographic structure of hydroxyapatite was determined by Rietveld structural refinement of the XRD data, as shown in **Table 2**. In agreement with Gibson et al. [11], sintered silicon substitution resulted in a decrease in the a-axis and an increase in the c-axis of the unit cell as compared to stoichiometric hydroxyapatite, with little effect on the volume of the unit cell.

Table 2 • Unit cell parameters for sintered HA and SA powder samples as determined by the analysis of XRD data

Samples	a/Å	c/Å	Unit cell volume/Å³
HA Sintered	9.4215(4)	6.8829(5)	529.118(4)
SA Sintered	9.418(1)	6.888(1)	529.26(1)

3.3. Fourier transform infrared-photoacoustic spectroscopy (FTIR-PAS)

FTIR spectroscopy was performed to study the powders in the precipitated state and after sintering to evaluate the effect of silicate substitution on the key functional groups of hydroxyapatite, such as hydroxyl and phosphate. **Figures 3** and **4** show the FTIR spectra of the HA and SA powders, respectively. The spectra of the HA and SA precipitates were found to be quite similar, where a weak OH band at $3{,}570$ cm^{-1} was partially obscured by a broad band between $2{,}500$ and $2{,}700$ cm^{-1}, which is characteristic of adsorbed water in the sample. Characteristic phosphate bands were also observed at around $1{,}090$ and $1{,}030$ cm^{-1} for v_3 vibration modes, 960 cm^{-1} for v_1 mode, and 600, 630, and 560 cm^{-1} for v_4 modes [11]. In addition, bands associated with carbonate groups at $1{,}650$, $1{,}455$, and $1{,}415$ cm^{-1} were also identified in both precipitate powders with a band at 875 cm^{-1} also being clearly visible in the HA precipitate. The spectra of the sintered powders showed some key differences from the precipitates, in both the HA and SA sintered samples, the broad band due to moisture and the bands attributed to carbonate disappeared, while bands appeared in the $2{,}000$–$2{,}200$ cm^{-1} region for both sintered samples, which may be attributed to the surface-adsorbed HPO_4 groups. Comparing the spectra of the sintered HA and SA, notable differences were changes in the phosphate bands between $900^{-1}{,}100$ and 500–700 cm^{-1}; the spectra showed the same bands, but the ratio and definition of the peak heights varied. Moreover, additional bands were observed at 850 and 755 cm^{-1} in the spectrum of the sintered SA.
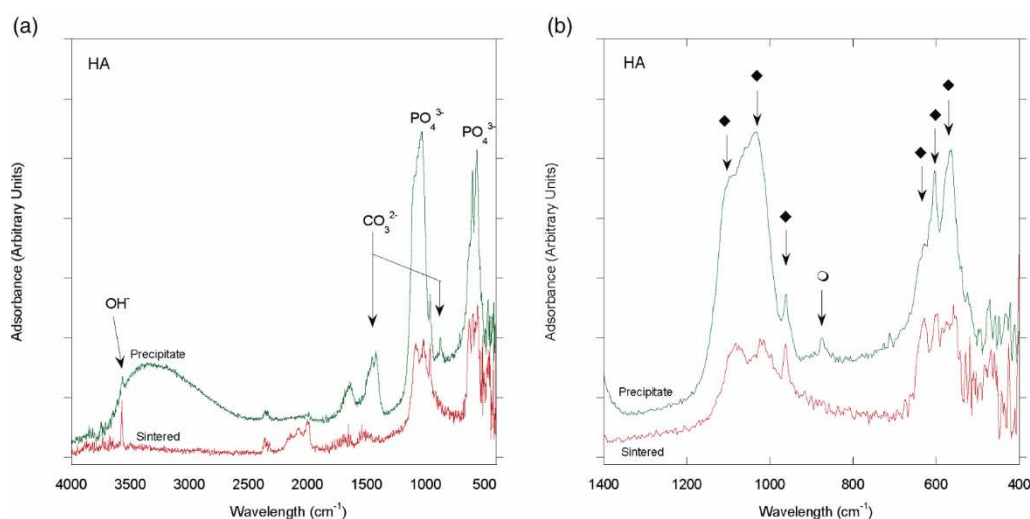

Figure 3 • FTIR-PAS spectra of HA powders shown as (a) full and (b) short ranges, where bands marked with ◆ are attributed to phosphate and ○ are attributed to carbonate.
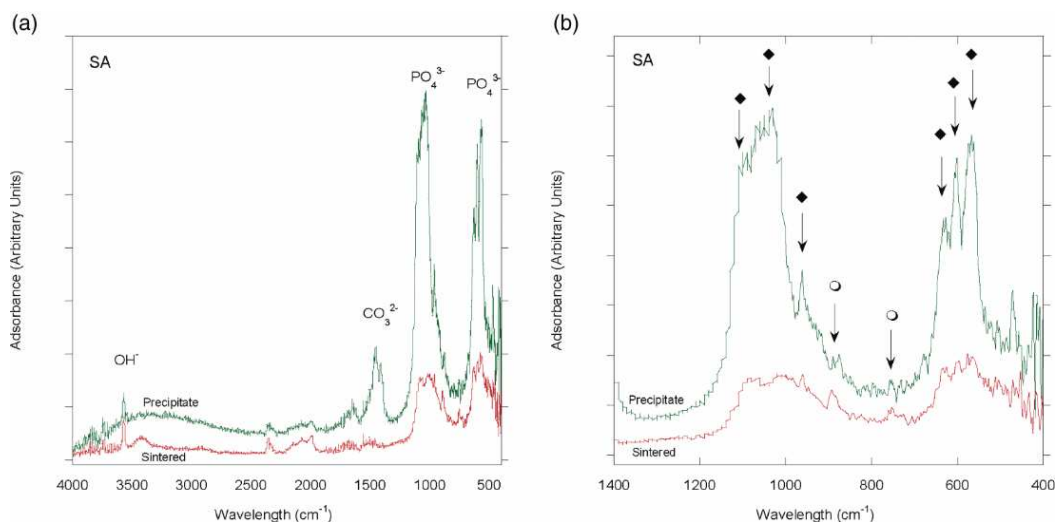
Figure 4 • FTIR-PAS spectra of SA powders shown as (a) full and (b) short ranges, where bands marked with ◆ are attributed to phosphate and ○ indicate new bands in the sintered SA powder.

3.4. Solid-state nuclear magnetic resonance spectroscopy

Figure 5 shows the ^{31}P response spectra for HA as precipitate (**Figure 5a**), calcined (**Figure 5c**), and sintered samples at 1,250°C (**Figure 5e**) as compared to SA precipitate (**Figure 5b**), calcined (**Figure 5d**), and sintered samples at 1,300°C (**Figure 5f**). There was no significant variation in the appearance of spectra obtained between the HA and SA precipitate or calcined powders. Both HA and SA precipitate and calcined powders exhibited a single resonance at 2.8 ppm typical of a PO_4 environment; however, in sintered SA powders, a split in the resonance at 4.58 ppm was observed, representative of a second phosphate environment, whereas sintered HA powders continued to exhibit only one resonance.
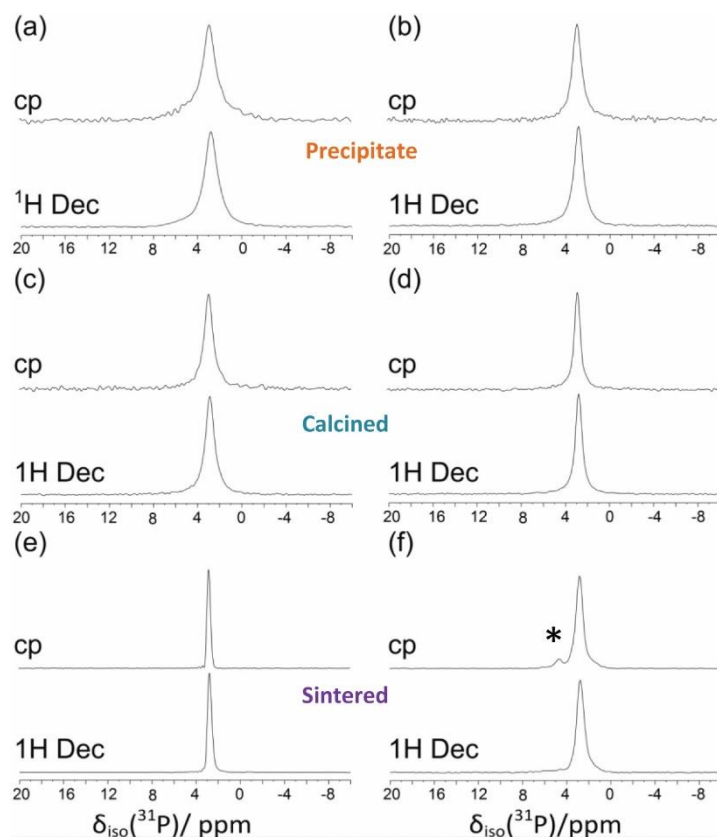

Figure 5 • CPMAS and proton-decoupled (^{1}H dec) one-pulse ^{31}P spectrum of (a) HA precipitate, (b) SA precipitate, (c) HA calcined, (d) SA calcined, (e) sintered HA, and (f) sintered SA. *Marks the split in the phosphate resonance observed only in sintered SA powders.

Figure 6 shows the resulting ^{29}Si probe spectra obtained from the as-precipitated (**Figure 6a**), calcined (**Figure 6b**) and sintered SA powders (**Figure 6c**), demonstrating a single resonance indicating the presence of a silicate environment. Additionally in **Figure 6c** showing the spectra obtained from the sintered sample, some side bands are observed.

Table 3 shows the chemical shifts observed by the powder samples for both ^{29}Si and ^{31}P resonances depicted as numerical values from that observed in **Figures 5** and **6**, respectively. Peak widths were observed to decrease with increasing powder heat treatment for both ^{29}Si and ^{31}P resonances.
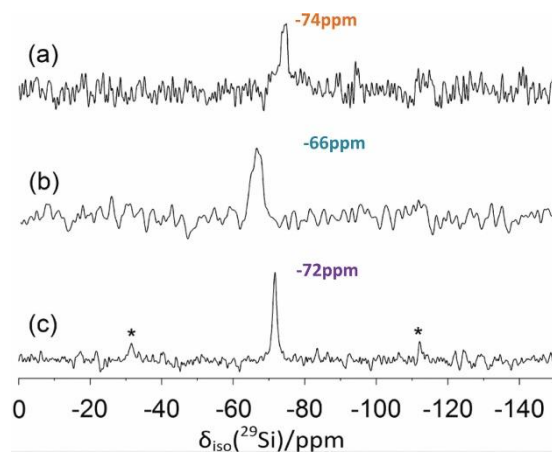
Figure 6 • The CPMAS ^{29}Si spectra of (a) SA precipitate, (b) SA calcined, and (c) SA sintered; all are orthosilicate of the Q_0 environment. *Denotes the spinning sidebands.

Table 3 • Isotropic chemical shifts for ^{29}Si and ^{31}P resonances

Sample	Experiment	$\delta_{iso}(^{29}Si)$/ppm	FWHM/Hz	$\delta_{iso}(^{31}P)$/ppm	FWHM/Hz
HA as precipitated	CP	-	-	2.93	290
	^{1}H dec			2.91	280
HA calcined	CP	-	-	2.80	130
	^{1}H dec			2.79	150
HA sintered	CP	-	-	2.81	80
	^{1}H dec			2.81	90
SA as precipitated	CP	-74.30^a	920	2.86	200
	^{1}H dec			2.86	200
SA calcined	CP	-66.00	440	2.88	190
	^{1}H dec			2.87	190
SA sintered	CP	-71.70	130	2.87(m), 4.75	150(m), 120
	^{1}H dec			2.83	160

FWHM, full width half maximum; m, major component.
^{a}Center of gravity taken due to dispersion of chemical sites.

4. Discussion

Adsorption of protein on apatite depends largely on the surface area and physiochemical properties (such as surface charge and hydrophobicity) of the apatite after the sintering processes [39]. Hydrophobicity is highly dependent on surface roughness and intrinsic chemistry, which is why the impact of ionic substitution on both the grain and crystallographic structures in any bioceramic is of biological significance, as it is the composition and conformation of the protein interlayer that directs the cell response [40].

In HA, a Ca/P molar ratio of 1.67 is required for the formation of a stoichiometric HA as a single-phase product. When the Ca/P ratio is higher than 1.67, in the absence of any other ionic groups capable of occupying the phosphate sites, the HA will decompose when sintered to form a second phase of calcium oxide (CaO), significantly altering the intrinsic chemistry of the material, which has been shown to compromise the bioactivity [41].

A similar molar ratio on the design Ca/(P + Si) of 1.67 is also required when forming phase-pure SA [11, 37]. This mirrors the well-documented change in the molar ratio of Ca/P observed when carbonate-substituted HA is produced where a Ca/(P + C)

of 1.67 is required for phase purity [42, 43]. Gibson et al. studied the effect of sintering carbonated HA (CHA) as compared to HA under a range of atmospheres and temperatures, and demonstrated that in a dry air atmosphere as-precipitated phosphate-deficient CHA begins to decompose into CaO and HA with the loss of carbonate ions, between 750 and 900°C [44], as the apatite transforms from being poorly crystalline to highly crystalline. On the contrary, in a CO_2 atmosphere, this decomposition effect was not observed for any of the phosphate-deficient CHAs studied, thus validating that if the loss of carbonate ions can be prevented during the sintering process, a phase-pure sintered carbonate-substituted apatite was formed if the appropriate molar ratios were retained.

4.1. Chemical interpretations through XRF, XRD, and FTIR

Elemental analysis of the stoichiometric hydroxyapatite (HA) and 0.8wt% Si containing silicate-substituted hydroxyapatite (SA) powders produced via aqueous precipitation routes based on the methods of Gibson et al. [11] confirmed a good agreement between the design and measured values of the final products (**Table 1**). The key difference between HA and SA being the design Ca/P molar ratios of 1.67 and 1.76, respectively, calculated

to retain the parity between the Ca/(P + Si) molar ratios of HA and SA at 1.67 if a phase-pure apatitic chemistry is to be preserved in SA containing 0.8wt% Si. XRD analysis of the as-precipitated, calcined, and sintered powders demonstrated that the apatitic phase purity was maintained in precipitate and heat-treated powders for both HA and SA (**Figure 2**). All peaks in the HA and SA patterns corresponded to the ICDD pattern for stoichiometric hydroxyapatite, despite the non-stoichiometric Ca/P ratio of 1.76 in the SA as determined by XRF. Apatite precipitates with a non-stoichiometric Ca/P ratio of 1.76 would be expected upon heat treatment to decompose to yield 3.0wt% CaO, where CaO is a more likely decomposition product than CaOH at elevated temperatures in a dry air atmosphere [44]. A quantity of 3.0wt% CaO is well within the detection limits of XRD and should form a clear peak on the XRD pattern at $37°$ 2θ [41]. This was not observed at a temperature of either 700°C or 1,300°C.

FTIR spectroscopy of the precipitate and sintered powders demonstrated the presence of hydroxyl and phosphate groups within both HA and SA, as expected, along with additional bands in the SA spectra that could be attributed to silicate group vibrations [45]. Again, considering the XRD patterns, where there is no evidence of a second phase, the circumstantial evidence points to the silicate groups from the FTIR spectra being incorporated within the apatite lattice [1]. Until now, these three analyses together have been used as evidence to support the theory that the non-stoichiometric hydroxyapatite powder produced in the presence of a balanced level of silicon via this route is silicate-substituted hydroxyapatite, where the silicate is site-specifically substituted for phosphate within the crystallographic structure of the hydroxyapatite. This assumption was based on the fact that an apatitic precipitate with a defective or non-stoichiometric Ca/P molar ratio greater than 1.67 would, on sintering, normally be expected to decompose to a biphasic mixture of hydroxyapatite and calcium oxide. The fact that on sintering, a non-stoichiometric apatite with a Ca/P molar ratio greater than 1.67 but synthesized in the presence of sufficient silicon to yield a molar Ca/(P + Si) ratio of 1.67 maintained phase purity, was believed to demonstrate that decomposition was inhibited by the site-specific substitution of silicate for phosphate groups into the apatite lattice, stabilizing the apatitic structure in the absence of sufficient phosphate. Gibson et al. also presented evidence through analysis of hydroxyl occupancy that the number of hydroxyl groups was decreased when non-stoichiometric apatites were synthesized in the presence of silicon, suggesting that the OH- groups were lost so as to maintain the charge balance upon substitution of SiO_4^{4-} groups for PO_4^{3-} groups [11]. Moreover, the appearance of extra bands in the FTIR spectra of SA as compared to HA [1, 11, 46, 47] at wavelengths associated with silicate vibrations [45] provided further evidence that silicate groups were present within SA. However, although compelling, all this evidence remains circumstantial and are subject to dispute.

4.2. NMR interpretations: ^{31}P and ^{29}Si analysis

The CPMAS and proton-decoupled phosphorus SSNMR results show a single-pronounced resonance at 2.8 ppm for all the samples, which is typical for hydroxyapatite. This peak is representative of the PO_4 environment in hydroxyapatite. There is a decrease in the peak width as you move from the precipitate samples to the sintered samples; this indicates less dispersion of the local PO_4 sites, reflecting the increased levels of crystallinity and order expected within the calcined and sintered powders.

However, in the sintered SA sample (**Figure 5f**), a split in the phosphate resonance was observed at 4.58 ppm, which is representative of the presence of a secondary phosphate environment, indicating the presence of an additional chemical environment in close proximity. The ratio of the two resonances was found to be 1:14.

The ^{29}Si CPMAS results show a single resonance which appears at −74.30 ppm for the SA precipitated sample, −66.00 ppm for the SA calcined sample, and −71.70 ppm for the sintered SA sample (as shown in **Figure 6** and **Table 3**). As observed in the ^{31}P results, the width of the peak decreases with increasing sample processing, indicating that the silicon environments are becoming less dispersed. Gasqueres and colleagues have observed a resonance at −72.8 ppm throughout their tri-phase mixtures of HA, TCP, and various wt% Si and attributed this to be a Q_0 silicon environment [33, 48] within the HA phase. Recently, MacDonald has shown that Q_0 silicon species in β-tricalcium phosphate (βTCP) form between −68 and −74 ppm [49]. Although the calcined results appear outside this defined region, we are confident to confirm that all three samples had Q_0 silicate environments and indicate that the uptake of silicon was successful during the SA synthesis and retained during subsequent heat treatment. Moreover, the split in the phosphate resonance, evident in the sintered SA as the sample crystallinity increases, suggests that the silicate is in close proximity to the phosphate environment. As NMR is an inherently surface-insensitive technique, resulting from signal broadening due to the limited translational symmetry at surfaces, the observed ^{29}Si resonance can be confirmed to be evidence of the uptake of silicon into the bulk apatite structure.

5. Conclusions

Using SSNMR has enabled incorporation of low levels of silicon element in a silicate-substituted hydroxyapatite to be successfully located in the bulk apatite structure. This analysis corroborates the circumstantial findings obtained through combined use of elemental analysis via XRF, phase identification via XRD, and ionic species analysis via FTIR spectroscopy to support the premise that silicate is site-specifically substituted for phosphate into the apatite lattice of silicate-substituted hydroxyapatite, rather than being present as a second amorphous phase at grain boundaries. This observation may be key to understanding the mechanisms by which the introduction of 0.8wt% silicon enhances bone regeneration in apatitic bone graft substitute materials.

Author contributions

Conceptualisation: MM and KH; methodology: KH, MM, RW, GR; software: RW, GR, PG; formal analysis: MM, RW, GR; investigation: MM, GR, RW; resources: KH, AS, PG; data curation: MM, RW, GR; writing original draft prep: MM; writing review and editing: KH, MM, AS, GR; visualisation: KH, MM, GR, RW; supervision: KH, AS; project admin: MM, KH, AS; funding: KH.

Conflict of interest

The authors declare no conflict of interest.

Data availability statement

Data supporting these findings are available within the article, at https://doi.org/10.20935/AcadMatSci6121, or upon request.

Institutional review board statement

Not applicable.

Informed consent statement

The authors declare no human participants were involved in this study.

Sample availability

Samples can be accessed via Dr Karin Hing in SEMS at Queen Mary University of London as they are still used for the remaining of the research group through her permission.

Additional information

Publisher's note

Copyright

References

1. Hing KA, Revell PA, Smith N, Buckland T. Effect of silicon level on rate, quality and progression of bone healing within silicate-substituted porous hydroxyapatite scaffolds. Biomaterials. 2006;27:5014–26.

2. Jenis LG, Banco RJ. Efficacy of silicate-substituted calcium phosphate ceramic in posterolateral instrumented lumbar fusion. Spine. 2010;35(20):E1058–63.

3. Nagineni VV, et al. Silicate-substituted calcium phosphate ceramic bone graft replacement for spinal fusion procedures. Spine. 2012;37(20):E1264–72.

4. Pimenta L, Marchi L, Oliveira L, Coutinho E, Amaral R. A prospective, randomized, controlled trial comparing radiographic and clinical outcomes between stand-alone lateral interbody lumbar fusion with either silicate calcium phosphate or rh-BMP-2. J Neurol Surg A. 2013;74(6):343–50.

5. Carlisle EM. Silicon-essential element for chick. Science. 1972;178(4061):619–21.

6. Carlisle EM. Silicon: a requirement in bone formation independent of vitamin D1. Calcif Tissue Int. 1981;33(1):27–34.

7. Schwartz K. Growth-promoting effects of silicon in rats. Nature. 1972;239(5371):333–4.

8. Schwartz K. A bound form of silicon in glycosaminoglycans & polyuronides. Proc Nat Acad Sci. 1973;70:1608–12.

9. Hench L, Paschall H. Direct chemical bond of bioactive glass-ceramic materials to bone and muscle. J Biomed Mater Res. 1973;7(3):25–42.

10. Xynos ID., Edgar AJ, Buttery LD, Hench LL, Polak JM. Ionic products of bioactive glass dissolution increase proliferation of human osteoblasts and induce insulin-like growth factor II mRNA expression and protein synthesis. Biochem Biophys Res Commun. 2000;276(2):461–5.

11. Gibson IR, Best SM, Bonfield W. Chemical characterization of silicon-substituted hydroxyapatite. J Biomed Mater Res. 1999;44(4):422–8.

12. Botelho CM, Lopes MA, Gibson IR, Best SM, Santos JD. Structural analysis of Si-substituted hydroxyapatite: zeta potential and X-ray photoelectron spectroscopy. J Mater Sci Mater Med. 2002;13:1123–7.

13. Gibson IR, Best SM, Bonfield W. Effect of silicon substitution on the sintering and microstructure of hydroxyapatite. J Am Ceram Soc. 2002;85(11):2771–7.

14. Patel N., et al. A comparative study on the *in vivo* behaviour of hydroxyapatite and silicon substituted hydroxyapatite granules. J Mater Sci Mater Med. 2002;13:1199–206.

15. Botelho CM, et al. Human osteoblast response to silicon-substituted hydroxyapatite. J Biomed Mater Res A. 2006; 79(3):723–30.

16. Guth K, Buckland T, Hing KA. Silicon dissolution from microporous silicon substituted hydroxyapatite and its effect on osteoblast behaviour. Key Eng Mater. 2006;309-311:117–20.

17. Porter AE, Buckland T, Hing KA, Best SM, Bonfield W. The structure of the bond between bone and porous silicon-substituted hydroxyapatite bioceramic implants. J Biomed Mater Res. 2006;78A:25–33.

18. Rashid N, Harding IS, Buckland T, Hing KA. Nano-scale manipulation of silicate-substituted apatite chemistry impacts surface charge, hydrophilicity, protein adsorption and cell attachment. Int J Nano Biomater. 2008;1(3):299–319.

19. Thomas CH, et al. The role of vitronectin in the attachment and spatial distribution of bone-derived cells on materials with patterned surface chemistry. J Biomed Mater Res. 1997;37:81–93.

20. Yin G, Liu Z, Zhan J, Ding FX, Yuan NJ. Impacts of the surface charge property on protein adsorption on hydroxyapatite. Chem Eng J. 2002;87(2):181–6.

21. Mafina M-K, Sullivan AC, Hing KA. Use of a fluorescent probe to monitor the enhanced affinity of rh-BMP-2 to silicated-calcium phosphate synthetic bone graft substitutes under competitive conditions. Mater Sci Eng C. 2017;80: 207–12.

22. Guth K, Campion C, Buckland T, Hing KA. Effect of silicate-substitution on attachment and early development of human osteoblast-like cells seeded on microporous hydroxyapatite discs. Adv Eng Mater. 2010;12(1–2):B26–36.

23. Guth K, Campion C, Buckland T, Hing KA. Surface physiochemistry affects protein adsorption to stoichiometric and silicate-substituted microporous hydroxyapatites. Adv Eng Mater. 2010;12(4):B113–21.

24. Porter AE, Best SM, Bonfield W. Ultrastructural comparison of hydroxyapatite and silicon-substituted hydroxyapatite for biomedical applications. J Biomed Mater Res. 2004;68A: 133–41.

25. Porter AE, Patel N, Skepper JN, Best SM, Bonfield W. Comparison of in vivo dissolution processes in hydroxyapatite and silicon-substituted hydroxyapatite bioceramics. Biomaterials. 2003;24:4609–20.

26. Christophy C, Rashid N, Di Silvio L, Hing KA. Encouraging nature with ceramics: the roles of surface roughness and physio-chemistry on cell response to substituted apatites. Adv Sci Technol. 2008;57:22–30.

27. Wilson RM, Elliot JC, Dowker SEP, Smith RI. Rietveld structure refinement of precipitated carbonate apatite using neutron diffraction data. Biomaterials. 2004;25:2205–13.

28. Wilson RM, Elliot JC, Dowker SEP, Rodriguez-Lorenzo LM. Rietveld refinements and spectroscopic studies of the structure of Ca-deficient apatite. Biomaterials. 2005;26: 1317–27.

29. Flewitt PEJ, Wild RK. Physical methods for materials characterisation. 2nd ed. Bristol & Philadelphia: IOP Publishing Ltd; 2003.

30. Isobe T, Nakumura S, Nemoto R, Senna M. Solid-state double nuclear magnetic resonance study of the local structure of calcium phosphate nanoparticles synthesized by a wet-mechanochemical reaction. J Phys Chem B. 2002;106: 5169–76.

31. Gervais C, et al. New perspectives on calcium environments in inorganic materials containing calcium-oxygen bonds: a combined computational-experimental ^{43}Ca NMR approach. Chem Phys Lett. 2008;464:42–8.

32. Laurencin D, Wong A, Dupree R, Smith ME. Natural abundance ^{43}Ca solid state NMR characterisation of hydroxyapatite: identification of the two calcium sites. Magn Reson Chem. 2008;46:347–50.

33. Gasqueres G, et al. Revisiting silicate substituted hydroxyapatite by solid state NMR. Magn Reson Chem. 2008;46:342–6.

34. Andreev AS, et al. Solid-state NMR and computational insights into the crystal structure of silicocarnotite-based bioceramic materials synthesised mechanochemically. Solid State Nucl Magn Reson. 2017;84:151–7.

35. Akao M, Aoki H, Kato K. Mechanical properties of sintered hydroxyapatite for prosthetic applications. J Mater Sci. 1981; 16:809–12.

36. Holland TJB, Redfern SAT. Unicell refinement from powder diffraction data: the use of regression diagnostics. Mineral Mag. 1997;61:65–77.

37. Hing KA, Gibson IR, Di-Silvio L, Best SM, Bonfield W. Effect of variation in Ca:P ratio on cellular response of primary human osteoblast-like cells to hydroxyapatite-based ceramics. Bioceramics. 1998;11:293–6.

38. Mostafa NY. Characterization, thermal stability and sintering of hydroxyapatite powders prepared by different routes. Mater Chem Phys. 2005;94(2–3):333–41.

39. Wilson JC, Clegg RE, Leavesley DI, Pearcy MJ. Mediation of biomaterial-cell interactions by adsorbed proteins: a review. Tissue Eng. 2005;11(1/2):1–18.

40. Anselme K, et al., The relative influence of the topography and chemistry of TiAl6V4 surfaces on osteoblastic cell behaviour. Biomaterials. 2000;21:1567–77.

41. Hing KA, Gibson IR, Revell PA, Best SM, Bonfield W. Influence of phase purity on the *in vivo* response to hydroxyapatite. Key Eng Mater. 2001;192–195:373–6.

42. Gibson IR, Bonfield W. Novel synthesis and characterization of an AB-type carbonate-substituted hydroxyapatite. J Biomed Mater Res. 2002;59:697–708.

43. Barralet JE, Best SM, Bonfield W. Effect of sintering parameters on the density and microstructure of carbonate hydroxyapatite. J Mater Sci Mater Med. 2000;11:719–24.

44. Merry JC, Gibson IR, Best SM, Bonfield W. Synthesis and characterization of carbonate hydroxyapatite. J Mater Sci Mater Med. 1998;9:779–83.

45. Dorschner J. Infrared spectra of silicate grains. Astron Nachr Bd. 1971;293*(H)*:53–5.

46. Balas F, Perez-Pariente J, Vallet-Regi M. In vitro bioactivity of silicon-substituted hydroxyapatites. J Biomed Mater Res. 2003;66 A:364–75.

47. Thian ES, et al. Silicon-substituted hydroxyapatite (SiHA): A novel calcium phosphate coating for biomedical applications. J Mater Sci. 2006;41:709–17.

48. Hayakawa S, et al. Heterogeneous structure and in vitro degradation behaviour of wet-chemically derived nano-crystalline silicon-containing hydroxyapatite particles. Acta Biomaterialia. 2013;9:4856–67.

49. Duncan J, et al. Furthering the understanding of silicate-substitution in a-tricalcium phosphate: an X-ray diffraction, X-ray fluorescence and solid state nuclear magnetic resonance study. Acta Biomaterialia. 2014;10:1443–50.